Scripta Materialia 252 (2024) 116260

Contents lists available at ScienceDirect

Scripta Materialia

journal homepage: www.journals.elsevier.com/scripta-materialia

Design and development of a novel non-equiatomic Ti-Nb-Mo-Ta-W refractory high entropy alloy with a single-phase body-centered cubic structure

Yong Seong Kim [a,1], Ryosuke Ozasa [a,b,1], Kazuhisa Sato [c], Ozkan Gokcekaya [a,b], Takayoshi Nakano [a,b,*]

[a] Division of Materials and Manufacturing Science, Graduate School of Engineering, Osaka University, 2-1 Yamadaoka, Suita, Osaka 565-0871, Japan
[b] Anisotropic Design and Additive Manufacturing Research Center, Osaka University, 2-1 Yamadaoka, Suita, Osaka 565-0871, Japan
[c] Research Center for Ultra-High Voltage Electron Microscopy, Osaka University, 7-1 Mihogaoka, Ibaraki, Osaka 567-0047, Japan

ARTICLE INFO

Keywords:
Refractory high entropy alloys (RHEAs)
Casting
Segregation
CALPHAD
Microstructure

ABSTRACT

Element segregation and consequent phase separation are challenging problems in refractory high entropy alloys (RHEAs). In this study, thermodynamic parameters and calculation of phase diagrams (CALPHAD) were implemented for RHEA design to suppress segregation and phase separation. A novel non-equiatomic RHEA, $Ti_1(NbMoTa)_2W_{0.5}$ alloy, was designed with a minimized difference between liquidus and solidus temperatures (ΔT_{l-s}) and a wide temperature range between solidus temperature and transformation temperature (ΔT_{single}) and compared with equiatomic RHEA. As-cast $Ti_1(NbMoTa)_2W_{0.5}$ alloy maintained a single-phase body-centered cubic (BCC) structure, corresponding to the Scheil–Gulliver model, and segregation of constituent elements was suppressed owing to the minimized ΔT_{l-s}. $Ti_1(NbMoTa)_2W_{0.5}$ alloy showed excellent strength (approximately 1100 MPa) and ductility (1.6 times higher than TiNbMoTaW alloy). This study demonstrated a novel approach for obtaining single-phase BCC-structured RHEAs with suppressed elemental segregation and phase separation by utilizing combined use of ΔT_{l-s} and ΔT_{single} as alloy design indexes.

Main body

High entropy alloys (HEAs) are a class of materials comprising 5–35 % of five or more elements at a mixing entropy greater than 1.5R (R: gas constant) [1]. HEAs are attracting attention as a next-generation material because of their excellent mechanical properties [2,3], corrosion resistance [4–6], fatigue properties [7,8], biocompatibility [9,10], and high-temperature stability [11,12], that originate from four core effects represented by the high entropy, lattice distortion, sluggish diffusion, and cocktail effects [13].

Most studies have focused on HEAs with equivalent compositions, where the constituent elements often segregate because of the super-multicomponent nature of the HEAs [9,14–16]. The segregation of constituent elements hinders the strengthening of the solid solution. It also induces phase separation and the formation of intermetallic compounds, degrading the inherent properties of the HEAs [17–19]. In particular, maintaining a single-phase solid solution over a wide temperature range is crucial for refractory HEAs (RHEAs). Recently, research on non-equiatomic HEAs has been attracting attention in order to improve the characteristics of HEAs. This alloy design effectively improved the properties of equiatomic HEAs with higher design flexibility [20–23]. In general, thermodynamic parameters and calculation of phase diagrams (CALPHAD) have been widely used for HEAs design [20,21].

This study investigated the alloy design and optimization of the composition using thermodynamic parameters and CALPHAD for RHEAs by focusing on the difference between liquidus and solidus temperatures (ΔT_{l-s}) [24] for suppression of elemental segregation and the temperature range between solidus temperature and transformation temperature (ΔT_{single}) [25] for phase stability. Furthermore, the designed alloy was fabricated via arc-melting, and its microstructure was investigated and compared with thermodynamic calculation results

* Corresponding author at: Division of Materials and Manufacturing Science, Graduate School of Engineering, Osaka University, 2-1 Yamadaoka, Suita, Osaka 565-0871, Japan.
E-mail address: nakano@mat.eng.osaka-u.ac.jp (T. Nakano).
[1] These authors contributed equally to this work.

https://doi.org/10.1016/j.scriptamat.2024.116260
Received 25 April 2024; Received in revised form 14 June 2024; Accepted 5 July 2024
Available online 11 July 2024

and simulations.

In this study, we determined the alloy composition in two steps: element selection and composition determination. The constituent elements were chosen from groups 4, 5, and 6 of the periodic table (which are classified as refractory materials). The atomic radius of the elements was considered first because it significantly impacts solid solution formation [26]. Therefore, four elements, Nb, Mo, Ta, and W, were selected as the base alloys for realizing a single-phase body center cubic (BCC) structure, owing to their close atomic radius differences. Additional elements were reviewed to realize HEAs having a mixing entropy (ΔS_{mix}) [26] exceeding 1.5R, as shown below:

$$\Delta S_{mix} = -R\sum_{i=1}^{n} x_i \ln x_i \quad (1)$$

Here, x_i is the mole fraction of the i-th element. Supplementary Fig. S1 shows (a) the pair enthalpy, (b) atomic radius, and (c) melting point of the constituent elements, which were examined to elucidate the interaction between each element. Among the elements in groups 4, 5, and 6, Ti has an atomic radius close to that of Nb, Mo, Ta, and W. The pair enthalpies between Ti and the elements are moderately close to zero, indicating a high probability of solid solution formation. Moreover, Ti exhibits the smallest valence electron concentration (*VEC*) value of 4. The *VEC* determines the ductility of BCC-structured HEAs; the smaller the *VEC*, the higher the ductility [27]. Furthermore, Nb, Mo, Ta, and W are commonly employed as BCC-phase-stabilizing elements in Ti-based alloys. Hence, a Ti-Nb-Mo-Ta-W alloy system was selected for this study.

The present strategies to obtain a solid solution and a stable single BCC phase involve minimizing ΔT_{l-s} and maintaining greater ΔT_{single}. It is expected to suppress segregation because solidification begins and ends within a narrow temperature range [24] and demonstrates good phase stability at high temperatures [25]. Thermodynamic parameters, including mixing enthalpy (ΔH_{mix}) [26], atomic radius mismatch (δ) [26], and melting point mismatch (ΔT_m) [25], were considered for predicting the formation of a solid solution. Details of the thermodynamic parameters used in this study are described in Appendix 2 of the *Supplementary information*. ΔH_{mix} represents the chemical compatibility between the constituent elements, with values close to zero indicating favorable conditions for the formation of solid solutions [26]. Both ΔH_{mix} and δ are crucial factors in predicting the formation of solid solutions in HEAs [28,29]. ΔT_m represents the extent of elemental interactions. The smaller the ΔT_m, the more readily the elements can be integrated into a lattice [30]. When its value is less than 16 %, a stable phase is maintained even at high temperatures [25]. Hence, to obtain a stable single BCC phase, we explored conditions that simultaneously

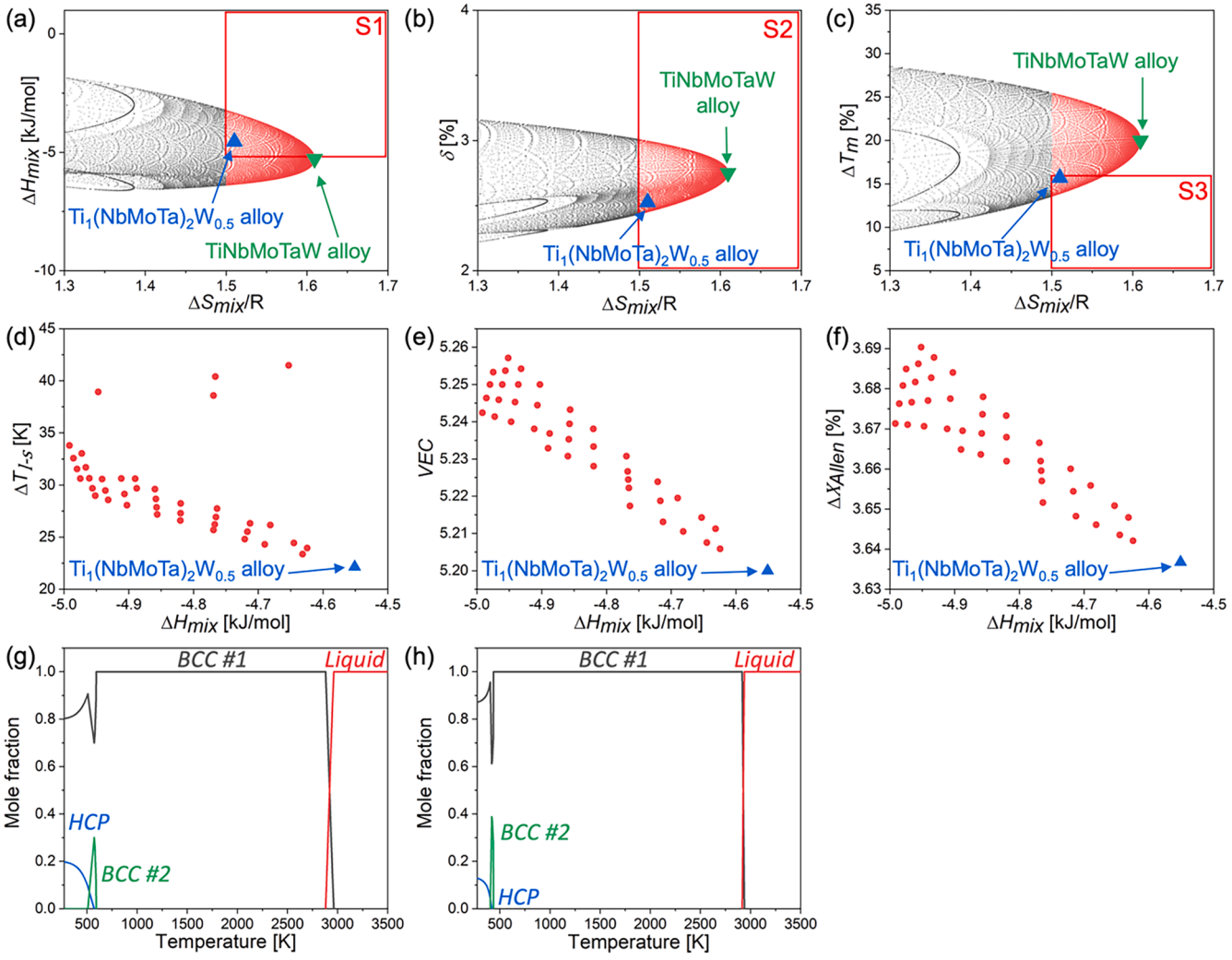

Fig. 1. (a) ΔH_{mix}, (b) δ, and (c) ΔT_m represented as functions of $\Delta S_{mix}/R$. The black dots indicate different alloy compositions. The red dots indicate the compositions with $\Delta S_{mix} \geq 1.5R$, which meet the conditions for HEA formation. The red rectangles denote the regions associated with indices S1 ($\Delta S_{mix} \geq 1.5R$ and $-5 \leq \Delta H_{mix} \leq 1$), S2 ($\Delta S_{mix} \geq 1.5R$ and $\delta \leq 6.6$), and S3 ($\Delta S_{mix} \geq 1.5R$ and $\Delta T_m \leq 16$). (d) ΔT_{l-s}, (e) *VEC*, and (f) $\Delta\chi_{Allen}$ as functions of ΔH_{mix} for the combinations that simultaneously meet the conditions of S1, S2, and S3. Equilibrium phase diagrams for the (g) TiNbMoTaW and (h) $Ti_1(NbMoTa)_2W_{0.5}$ alloys.

satisfied the following thresholds: $\Delta S_{mix} \geq 1.5R$, $-5 \leq \Delta H_{mix} \leq 5$, $\delta \leq 6.6$, and $\Delta T_m \leq 16$. In this study, to suppress the segregation of the constituent elements, they were categorized into three groups based on their melting point, as can be observed in the composition $Ti_x(NbMoTa)_yW_z$ in atomic % (at.%).

The thermodynamic parameters of the $Ti_x(NbMoTa)_yW_z$ were calculated and are presented in Fig. 1, wherein (a), (b), and (c) show the values of ΔH_{mix}, δ, and ΔT_m as functions of ΔS_{mix}, respectively. In this study, 29,790 composition combinations were evaluated. The black dots indicate the conditions where $\Delta S_{mix} < 1.5R$, whereas the red dots indicate the conditions satisfying the criteria $\Delta S_{mix} \geq 1.5R$. In addition, the areas enclosed in red squares, denoted as S1 ($\Delta S_{mix} \geq 1.5R$, $-5 \leq \Delta H_{mix} \leq 5$), S2 ($\Delta S_{mix} \geq 1.5R$, $\delta \leq 6.6$), and S3 ($\Delta S_{mix} \geq 1.5R$, $\Delta T_m \leq 16$), represent the conditions corresponding to a high probability of solid solution formation. Fig. 1 (d), (e), and (f) show the values of ΔT_{l-s}, *VEC* [31], and electronegativity ($\Delta\chi_{Allen}$) [32], respectively, for the compositions simultaneously satisfy S1, S2, and S3. The values are plotted as functions of ΔH_{mix}. From these results, we identified $Ti_1(NbMoTa)_2W_{0.5}$ alloy as the composition corresponding to the smallest ΔT_{l-s} as well as *VEC* and $\Delta\chi_{Allen}$. $\Delta\chi_{Allen}$ is a relevant factor in predicting intermetallic-compound formation, and solid solution formation is facilitated when $\Delta\chi_{Allen}$ is below 6 % [32]. Fig. 1(g) and (h) show the equilibrium phase diagram of the TiNbMoTaW and $Ti_1(NbMoTa)_2W_{0.5}$ alloys, respectively. The calculations were performed using the Thermo-Calc software [33] with the TCHEA5 database. Both alloys exhibited a high melting point above 2500°C and maintained a large ΔT_{single}. Hence, they are anticipated to demonstrate high phase stability even at high temperatures. It should be noted that $Ti_1(NbMoTa)_2W_{0.5}$ alloy exhibited greater ΔT_{single} and smaller ΔT_{l-s} than TiNbMoTaW alloy. The thermodynamic parameters for each composition are listed in Table 1.

Fig. 2(a, b) show the non-equilibrium solidification simulation results obtained using the Scheil–Gulliver model. The dotted lines represent equilibrium solidification, assuming infinitely fast diffusion in both the liquid and solid phases. The solid red lines indicate the Scheil–Gulliver model, which assumes infinitely fast diffusion in the liquid phase but no diffusion in the solid phase [34,35]. Both alloys exhibit a single BCC phase during non-equilibrium solidification. TiNbMoTaW alloy exhibits a significant difference between the equilibrium and non-equilibrium states as the solidification progresses. However, in $Ti_1(NbMoTa)_2W_{0.5}$ alloy, the difference between the equilibrium and non-equilibrium states remains small even as the solidification progresses, indicating an effective suppression of segregation. Moreover, compared to TiNbMoTaW alloy, $Ti_1(NbMoTa)_2W_{0.5}$ alloy exhibits a notably smaller ΔT_{l-s}. Fig. 2(a2, a3) and (b2, b3) show the compositional changes of the constituent elements in the liquid and solid phases during the non-equilibrium solidification of both alloys, respectively. In both alloys, the concentrations of high melting point elements (W and Ta) reduce during the initial stages of solidification in the liquid phase (Fig. 2(a2, b2)). This is because the high melting point element solidifies first due to the difference in melting point, forming a dendrite region. In the late stage of solidification, relatively low melting point elements (Ti and Nb) maintain a high mole fraction in the liquid and form an inter-dendrite region. Similarly, in the solid phase, the early-stage-solidified region exhibits a higher concentration of Ta and W, whereas the later-stage-solidified region displays a higher concentration of Ti and Nb (Fig. 2(a3, b3)). These results are consistent with the results of the distribution coefficient calculated at the liquidus temperature in the equilibrium state (Supplementary Table S1). The equilibrium distribution coefficient (k) can predict the segregation tendency and it was calculated using Thermo-Calc software. The k of Ta and W were above 1, indicating enrichment in the dendrite region, whereas the k of Ti, Nb were below 1, indicating enrichment in the inter-dendrite region [36,37]. However, the k-value of $Ti_1(NbMoTa)_2W_{0.5}$ alloy was closer to 1 than that of TiNbMoTaW alloy, indicating the suppression of segregation in $Ti_1(NbMoTa)_2W_{0.5}$ alloy.

Based on the alloy design, we fabricated TiNbMoTaW and $Ti_1(NbMoTa)_2W_{0.5}$ alloys via arc-melting. Details of the experimental methods are provided in Appendix 1 of the *Supplementary information*. Fig. 3(a) shows the X-ray diffraction (XRD) patterns, revealing the presence of a single BCC phase in both alloys, which is consistent with the non-equilibrium solidification simulation results (Fig. 2). From the XRD analysis, the lattice constants (a) of TiNbMoTaW and $Ti_1(NbMoTa)_2W_{0.5}$ alloys were determined to be 0.322 and 0.324 nm, respectively. Also a were calculated using Vegard's law based on the results of energy dispersive X-ray spectroscopy (EDS) analysis (Table 2) of the dendrite and inter-dendrite regions of both alloys (Supplementary Table S2). Only $Ti_1(NbMoTa)_2W_{0.5}$ alloy, the a measured by XRD and the calculated by Vegard's law at the dendrite and inter-dendrite regions were consistent (a_D=a_{ID}=0.324 nm) due to the suppressed segregation. Both alloys showed a doublet of the peak, which was attributed to the decomposition of Kα$_1$ and Kα$_2$ X-rays of the Cu target and not the formation of an additional phase. This can be seen from the fact that the intensity of the Kα$_1$ peak is approximately twice that of the Kα$_2$ peak. Fig. 3(c1, d1) show scanning electron microscopy-backscattered electron (SEM-BSE) images of the cross-sections of both alloys. Fig. 3(c2–c6, d2–d6) show the elemental mapping results of Ti, Nb, Mo, Ta, and W. The images reveal a dendrite structure comprising light-gray dendrite regions and dark-gray inter-dendrite regions. Both alloys show Ta- and W-rich phases with relatively high melting points in the dendrite region and Ti-, Nb-, and Mo-rich phases with relatively low melting points in the inter-dendrite region. Fig. 3(b) shows the partition coefficient $K = C_D/C_{ID}$ for the constituent elements, where C_D and C_{ID} are the average concentrations (at.%) in the dendrite and inter-dendrite regions, respectively. This has been widely used for quantitative segregation evaluation [38–40]. $K > 1$ and $K < 1$ indicate abundant elements in the dendrite and inter-dendrite regions, respectively (Table 2). In $Ti_1(NbMoTa)_2W_{0.5}$ alloy, K remains at approximately 1 for all elements, showing effective segregation suppression compared to TiNbMoTaW alloy as predicted by the calculations in the equilibrium and non-equilibrium states (Supplementary Table S1 and Fig. 2). These results suggested that the reduced ΔT_{l-s} suppresses elemental segregation.

Fig. 4 shows the results of the scanning transmission electron microscopy (STEM) and high-resolution TEM (HRTEM) observations for the inter-dendrite and dendrite regions of $Ti_1(NbMoTa)_2W_{0.5}$ alloy. The dendrite and inter-dendrite regions exhibit a uniform elemental distribution, indicating solid solution formation (Fig. 4(a1–a6) and (b1–b6)). The selected area electron diffraction (SAED) patterns represent a single BCC phase, which is consistent with the XRD analysis. No additional diffractions are observed. This indicates that no precipitate, such as B2, is formed in the regions (Fig. 4(a7, b7)). The (110) d-spacing measured from HRTEM images is 0.23 nm in both regions, indicating the suppression of segregation in the regions (Fig. 4(a8, b8)). Upon converting the d-spacing to a lattice constant, the resulting value is 0.325 nm, which agrees with the measurement obtained through XRD (a = 0.324 nm). These results confirmed the single phase of $Ti_1(NbMoTa)_2W_{0.5}$ alloy with suppressed segregation.

Table 1
Thermodynamic parameters of the TiNbMoTaW and $Ti_1(NbMoTa)_2W_{0.5}$ alloys.

Alloys	ΔS_{mix}/R	ΔH_{mix} [kJ/mol]	δ [%]	*VEC*	$\Delta\chi_{Allen}$ [%]	ΔT_m [%]	ΔT_{single} [K]	ΔT_{l-s} [K]
TiNbMoTaW	1.61	-5.3	2.75	5.2	3.6	20.0	2287.5	81.9
$Ti_1(NbTaMo)_2W_{0.5}$	1.51	-4.6	2.53	5.2	3.6	15.7	2479.9	22.2

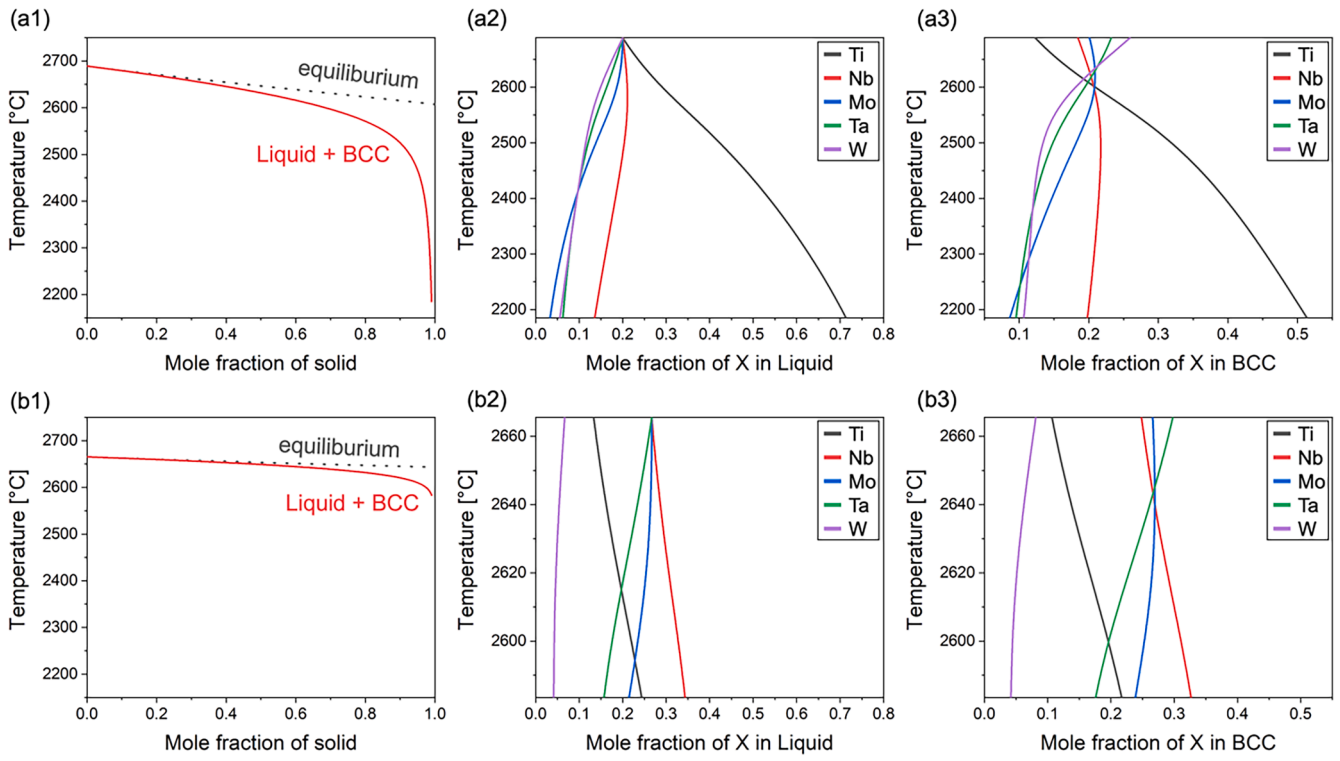

Fig. 2. Non-equilibrium solidification of the (a1) TiNbMoTaW and (b1) $Ti_1(NbMoTa)_2W_{0.5}$ alloys evaluated using the Scheil–Gulliver model. (a2, b2) Mole fraction of X in liquid, and (a3, b3) mole fraction of X in BCC (X = Ti, Nb, Mo, Ta, W).

Fig. 5(a) shows the compression test results, indicating the relationship between the true strain and true stress at 25°C for both alloys. The yield stress of the TiNbMoTaW alloy is 1211±52 MPa, which is higher than that of $Ti_1(NbMoTa)_2W_{0.5}$ alloy (1128±15 MPa). TiNbMoTaW alloy exhibits a fraction strain of 5.8±0.2 %, whereas $Ti_1(NbMoTa)_2W_{0.5}$ alloy exhibits a significantly higher fracture strain up to 9.1 ±0.1 %. BCC-structured HEAs show higher ductility at smaller *VEC* values [27]. The *VEC* value for the designed composition (*VEC*=5.2) is the same for both alloys. Additionally, both alloys have similar grain sizes (Supplementary Fig. S3). Therefore, the enhanced ductility of $Ti_1(NbMoTa)_2W_{0.5}$ alloy is attributed to the suppression of segregation, leading to a more uniform stress distribution during deformation [41]. Fig. 5(b) shows the correlation between the calculated yield strength ($\sigma_y^{cal.}$) and experimental yield strength ($\sigma_y^{exp.}$) for both alloys when considering the solid solution strengthening (SSS) effect ($\Delta\sigma_{ss}$) as a strengthening mechanism. Because both alloys were fabricated by arc-melting without deformation, dislocation strengthening was not considered. Moreover, there was no precipitation formation according to the XRD result (Fig. 3(a)); thus, precipitation strengthening was not relevant. Furthermore, the effect of grain-boundary strengthening was relatively small because of the large grain size and no significant difference in the alloys (Supplementary Fig. S3 and Supplementary Table S3). Based on the Hall–Petch relationship explained in Appendix 3 of the *Supplementary information*, the effect of grain-boundary strengthening ($\Delta\sigma_G$) was calculated as 44.7 MPa and 43.4 MPa in the TiNbMoTaW and $Ti_1(NbMoTa)_2W_{0.5}$ alloys, respectively. Therefore, in this study, SSS was considered as the main strengthening mechanism. $\Delta\sigma_{ss}$ was characterized using the model proposed by Senkov et al., which considers the interaction between HEA atoms in a BCC structure [42]. This model considers the atomic radius misfit (δ_i) and shear modulus misfit (η'_i) due to the multi-component nature of the HEA. This is expressed as follows [42]

$$\delta_i = \frac{9}{8}\sum X_j\delta_{ij} \tag{2}$$

$$\eta_i = \frac{9}{8}\sum X_j\eta'_{ij} \tag{3}$$

Here, δ_{ij} represents the difference in the atomic radii between elements i and j. η'_{ij} is related to η_{ij}, where $\eta_{ij} = 2(G_i - G_j)/(G_i + G_j)$ is the difference in shear modulus between elements i and j. Additionally, r_i, r_j, G_i and G_j are the atomic radii and shear modulus of elements i and j, respectively. X_j denotes the mole fraction of the i-th element. The $\Delta\sigma_{ss}$ for a BCC-structured HEA is expressed as follows [43].

$$\Delta\sigma_{ss} = B_i X_i^{2/3} \tag{4}$$

$$B_i = 3G\varepsilon_i^{4/3}Z \tag{5}$$

$$G = \sum G_i X_i \tag{6}$$

$$\varepsilon_i = \left(\eta'^{2}_i + \alpha^2\delta_i^2\right)^{1/2} \tag{7}$$

$$\eta'_i = \eta_i/(1 + |\eta_i|/2) \tag{8}$$

α in Eq. (7) indicates the difference in the interaction forces between the screw and edge dislocations and solute atom. For screw dislocations, the value of α is in the range of 3 – 16 and for edge dislocations, $\alpha \geq 16$ [44]. For BCC-structured HEAs, α=16 is often accepted because edge dislocations impact SSS more than screw dislocations [43]. Z is a fitting constant that was statistically determined as $Z = 0.0074$ [43]. Finally, $\Delta\sigma_{ss}$ (Eq. (4)) can be simplified as follows [43].

$$\Delta\sigma_{ss} = \frac{G}{45}\left(\sum \varepsilon_i^2 X_i\right)^{2/3} \tag{9}$$

Therefore, the calculated yield strength, $\sigma_y^{cal.}$ is expressed as follows.

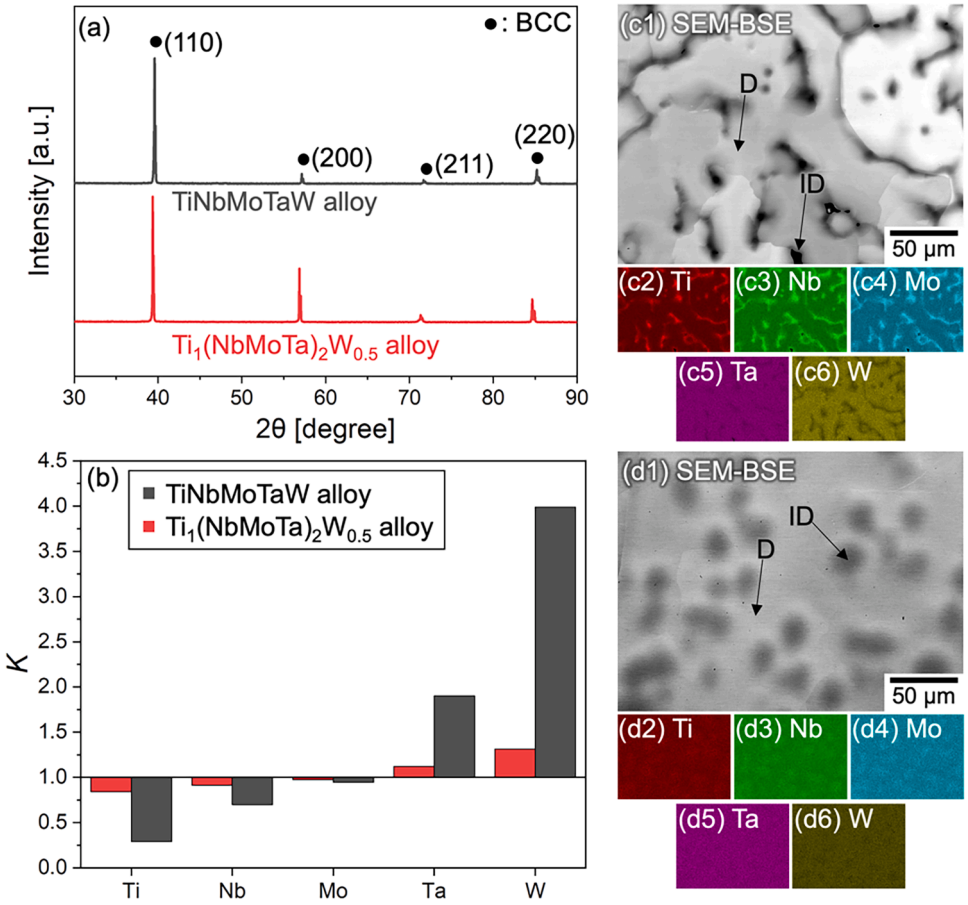

Fig. 3. Identification of crystal phase and microstructure of the TiNbMoTaW and $Ti_1(NbMoTa)_2W_{0.5}$ alloys developed via casting. (a) XRD profiles, (b) partition coefficient (K), (c, d) SEM-BSE images, and EDS elemental mapping images of (c1–c6) TiNbMoTaW and (d1–d6) $Ti_1(NbMoTa)_2W_{0.5}$ alloys. D and ID represent the dendrite and inter-dendrite regions, respectively in (c1) and (d1).

Table 2
Chemical compositions of the TiNbMoTaW and $Ti_1(NbMoTa)_2W_{0.5}$ alloys at the dendrite (D) and inter-dendrite (ID) regions in at.% and their partition coefficient ($K = C_D/C_{ID}$)

Composition (at.%)		Ti	Nb	Mo	Ta	W
TiNbMoTaW	C_D	9.7	17.6	20.2	25.2	27.2
	C_{ID}	33.4	25.2	21.4	13.3	6.8
	K	0.3	0.7	0.9	1.9	4.0
$Ti_1(NbTaMo)_2W_{0.5}$	C_D	11.1	25.7	26.4	28.7	8.3
	C_{ID}	13.2	28.0	27.0	25.5	6.3
	K	0.8	0.9	1.0	1.1	1.3

$$\sigma_y^{cal.} = \Delta\sigma_{ss} + (\sigma_y)_{mix} \quad (10)$$

Here, $(\sigma_y)_{mix}$ denotes the nominal yield strength, calculated as $(\sigma_y)_{mix} = \sum (\sigma_y)_i X_i$. $(\sigma_y)_i$ is the yield strength of the i-th element. Both alloys exhibited similar values of $(\sigma_y)_{mix}$. However, TiNbMoTaW alloy exhibited a higher value of $\Delta\sigma_{ss}$. This is because of the influence of shear modulus mismatch (G) in Eq. (6) ($G_{TiNbMoTaW}$=87.7 GPa, $G_{Ti_1(NbMoTa)_2W_{0.5}}$=78.7 GPa) and δ on SSS because δ plays a prominent role in SSS. However, when it exceeds a certain threshold, it can promote the formation of intermetallic compounds [20,32]. Therefore, carefully selecting an appropriate δ during HEA designing ($\delta \leq 6.6$ in the present study) is essential to achieve simultaneous phase stability and SSS.

In conclusion, we successfully developed a novel $Ti_1(NbMoTa)_2W_{0.5}$ alloy with excellent ductility and strength using thermodynamic parameters and CALPHAD. The $Ti_1(NbMoTa)_2W_{0.5}$ alloy exhibited a single-phase BCC structure and successfully suppressed segregation by minimized ΔT_{l-s} and greater ΔT_{single}, corresponding to CALPHAD simulations. It had higher room-temperature ductility than the TiNbMoTaW alloy while maintaining high strength. Because $Ti_1(NbMoTa)_2W_{0.5}$ alloy does not contain toxic elements [45], it can be proposed not only for high-temperature applications but also for biomedical applications owing to the expected improvement in corrosion resistance [46–48] and biocompatibility [49] with suppressed segregation. The potential of the $Ti_1(NbMoTa)_2W_{0.5}$ alloy as a refractory material and biomaterial will be studied in future work.

Role of the funding source

The funders of the study had no role in study design, data collection, data analysis, data interpretation, or writing of the report.

Funding

This work was partly supported by Grants-in-Aid for Scientific Research from the Japan Society for the Promotion of Science (JSPS) [grant numbers 22H01812, 22H05288 and 23H00235] and CREST-Nanomechanics: Elucidation of Macroscale Mechanical Properties based on Understanding Nanoscale Dynamics for Innovative Mechanical Materials ([grant number JPMJCR2194)] from the Japan Science and Technology Agency (JST).

Data statement

Data will be available upon reasonable request to the corresponding

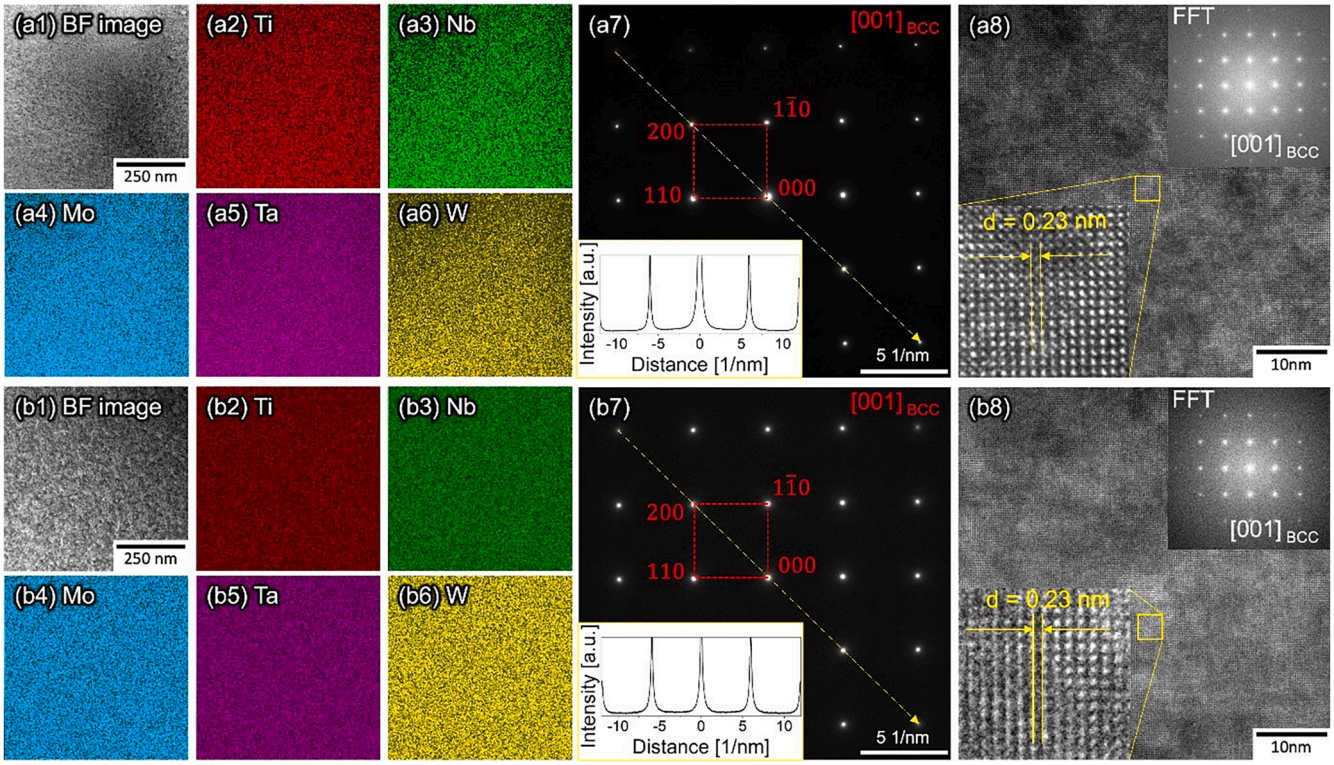

Fig. 4. Bright-field (BF) STEM images from (a1) dendrite and (b1) inter-dendrite regions of the $Ti_1(NbMoTa)_2W_{0.5}$ alloy; corresponding elemental distribution maps (a2–a6, b2–b6) obtained via STEM-EDS. SAED patterns obtained from (a7) dendrite and (b7) inter-dendrite regions along the [001] direction and intensity profile along the line (inset). HRTEM images of the (a8) dendrite and (b8) inter-dendrite regions in the [001] direction.

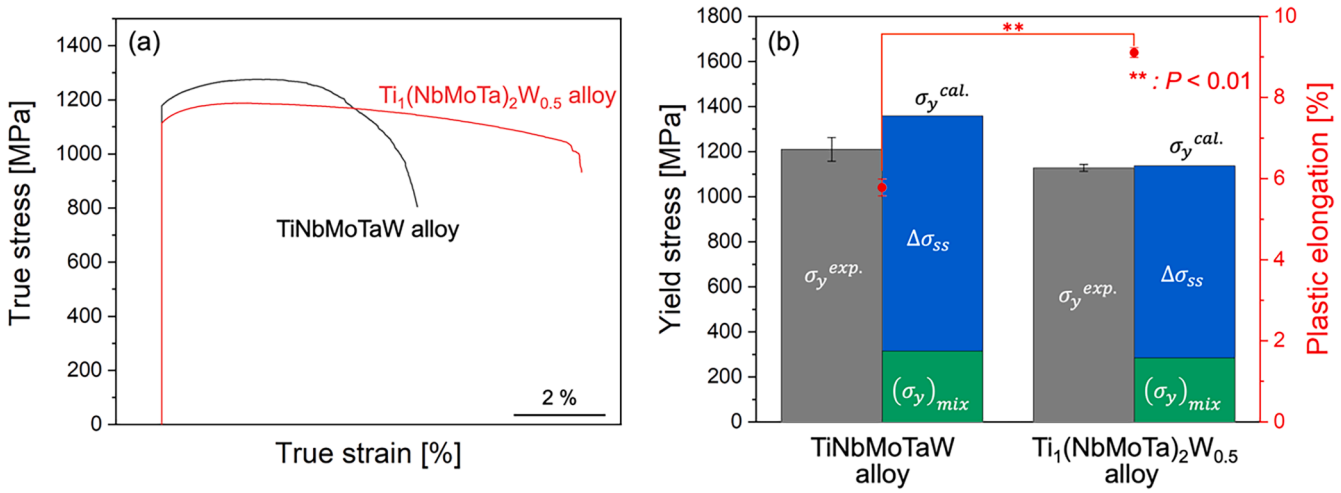

Fig. 5. (a) True stress-true strain curves obtained from the compression test at 25℃ on the TiNbMoTaW and $Ti_1(NbMoTa)_2W_{0.5}$ alloys. (b) Plastic elongation and comparisons between the calculated and experimentally obtained yield stress values. Combined contributions of the SSS ($\Delta\sigma_{ss}$) and nominal yield stress ($(\sigma_y)_{mix}$).

author.

CRediT authorship contribution statement

Yong Seong Kim: Writing – original draft, Software, Methodology, Investigation, Formal analysis. **Ryosuke Ozasa:** Writing – review & editing, Visualization, Project administration, Methodology, Investigation, Funding acquisition, Formal analysis, Data curation, Conceptualization. **Kazuhisa Sato:** Methodology, Formal analysis. **Ozkan Gokcekaya:** Writing – review & editing, Investigation, Formal analysis, Data curation. **Takayoshi Nakano:** Writing – review & editing, Validation, Supervision, Resources, Project administration, Funding acquisition.

Declaration of competing interest

The authors declare that they have no known competing financial interests or personal relationships that could have appeared to influence the work reported in this paper.

Supplementary materials

Supplementary material associated with this article can be found, in the online version, at doi:10.1016/j.scriptamat.2024.116260.

References

[1] J.W. Yeh, S.K. Chen, S.J. Lin, J.Y. Gan, T.S. Chin, T.T. Shun, C.H. Tsau, S.Y. Chang, Nanostructured high-entropy alloys with multiple principal elements: novel alloy design concepts and outcomes, Adv. Eng. Mater. 6 (5) (2004) 299–303, https://doi.org/10.1002/adem.200300567.

[2] S.H. Shim, H. Pouraliakbar, S.I. Hong, Hierarchical structured as-cast CrFeNiMn0.5Cu0.5 high entropy alloy with excellent tensile strength/ductility properties, Scr. Mater. 210 (2022) 114473, https://doi.org/10.1016/j.scriptamat.2021.114473.

[3] Y. Mu, L. He, S. Deng, Y. Jia, Y. Jia, G. Wang, Q. Zhai, P.K. Liaw, C.T. Liu, A high-entropy alloy with dislocation-precipitate skeleton for ultrastrength and ductility, Acta Mater. 232 (2022) 117975, https://doi.org/10.1016/j.actamat.2022.117975.

[4] S. Nene, M. Frank, K. Liu, S. Sinha, R. Mishra, B. McWilliams, K. Cho, Corrosion-resistant high entropy alloy with high strength and ductility, Scr. Mater. 166 (2019) 168–172, https://doi.org/10.1016/j.scriptamat.2019.03.028.

[5] F. Yoosefan, A. Ashrafi, S.M.M. Vaghefi, Corrosion and tribological behavior of CoCrFeMoNi high-entropy alloys as a potential vascular implant material, J. Alloy. Compd. 976 (2024) 172964, https://doi.org/10.1016/j.jallcom.2023.172964.

[6] X. Wen, X. Cui, G. Jin, Y. Liu, Y. Zhang, X. Zhang, E. Liu, H. Tian, Y. Fang, Corrosion and tribo-corrosion behaviors of nano-lamellar Ni1. 5CrCoFe0. 5Mo0. 1Nbx eutectic high-entropy alloy coatings: the role of dual-phase microstructure, Corrosion Sci. 201 (2022) 110305, https://doi.org/10.1016/j.corsci.2022.110305.

[7] X. Wang, W. Bai, Z. Zhang, Z. Wang, X. Ren, Enhanced fatigue resistance of a face-centered-cubic single-phase Al0. 3CoCrFeNi high-entropy alloy through planar deformation characteristic, Mater. Sci. Eng. A 862 (2023) 144499, https://doi.org/10.1016/j.msea.2022.144499.

[8] J. Hu, K. Yang, Q. Wang, Q.C. Zhao, Y.H. Jiang, Y.J. Liu, Ultra-long life fatigue behavior of a high-entropy alloy, Int. J. Fatigue 178 (2024) 108013, https://doi.org/10.1016/j.ijfatigue.2023.108013.

[9] M. Todai, T. Nagase, T. Hori, A. Matsugaki, A. Sekita, T. Nakano, Novel TiNbTaZrMo high-entropy alloys for metallic biomaterials, Scr. Mater. 129 (2017) 65–68, https://doi.org/10.1016/j.scriptamat.2016.10.028.

[10] S. San, P. Adhikari, R. Sakidja, J. Brechtl, P.K. Liaw, W.Y. Ching, Porosity modeling in a TiNbTaZrMo high-entropy alloy for biomedical applications, RSC Adv. 13 (51) (2023) 36468–36476, https://doi.org/10.1039/D3RA07313K.

[11] T.T. Shun, Y.C. Du, Age hardening of the Al0.3CoCrFeNiC0.1 high entropy alloy, J. Alloy. Compd. 478 (1-2) (2009) 269–272, https://doi.org/10.1016/j.jallcom.2008.12.014.

[12] K.Y. Tsai, M.H. Tsai, J.W. Yeh, Sluggish diffusion in Co–Cr–Fe–Mn–Ni high-entropy alloys, Acta Mater. 61 (13) (2013) 4887–4897, https://doi.org/10.1016/j.actamat.2013.04.058.

[13] J.W. Yeh, Alloy design strategies and future trends in high-entropy alloys, Jom 65 (2013) 1759–1771, https://doi.org/10.1007/s11837-013-0761-6.

[14] M. Wang, Z. Ma, Z. Xu, X. Cheng, Microstructures and mechanical properties of HfNbTaTiZrW and HfNbTaTiZrMoW refractory high-entropy alloys, J. Alloy. Compd. 803 (2019) 778–785, https://doi.org/10.1016/j.jallcom.2019.06.138.

[15] F.G. Coury, T. Butler, K. Chaput, A. Saville, J. Copley, J. Foltz, P. Mason, K. Clarke, M. Kaufman, A. Clarke, Phase equilibria, mechanical properties and design of quaternary refractory high entropy alloys, Mater. Des. 155 (2018) 244–256, https://doi.org/10.1016/j.matdes.2018.06.003.

[16] R. Ozasa, A. Matsugaki, T. Ishimoto, T. Nakano, Research and development of titanium-containing biomedical high entropy alloys (BioHEAs) utilizing rapid solidification via laser-powder bed fusion, Mater. Trans. 64 (1) (2023) 31–36, https://doi.org/10.2320/matertrans.MT-MLA2022011.

[17] L. Fang, J. Wang, X. Li, X. Tao, Y. Ouyang, Y. Du, Effect of Cr content on microstructure characteristics and mechanical properties of ZrNbTaHf0. 2Crx refractory high entropy alloy, J. Alloy. Compd. 924 (2022) 166593, https://doi.org/10.1016/j.jallcom.2022.166593.

[18] L. Liu, J. Zhu, C. Zhang, J. Li, Q. Jiang, Microstructure and the properties of FeCoCuNiSnx high entropy alloys, Mater. Sci. Eng. A 548 (2012) 64–68, https://doi.org/10.1016/j.msea.2012.03.080.

[19] X. Wang, Y. Zhang, Y. Qiao, G. Chen, Novel microstructure and properties of multicomponent CoCrCuFeNiTix alloys, Intermetallics 15 (3) (2007) 357–362, https://doi.org/10.1016/j.intermet.2006.08.005.

[20] V. Nguyen, M. Qian, Z. Shi, T. Song, L. Huang, J. Zou, Compositional design of strong and ductile (tensile) Ti-Zr-Nb-Ta medium entropy alloys (MEAs) using the atomic mismatch approach, Mater. Sci. Eng. A 742 (2019) 762–772, https://doi.org/10.1016/j.msea.2018.11.054.

[21] D. Ma, M. Yao, K.G. Pradeep, C.C. Tasan, H. Springer, D. Raabe, Phase stability of non-equiatomic CoCrFeMnNi high entropy alloys, Acta Mater. 98 (2015) 288–296, https://doi.org/10.1016/j.actamat.2015.07.030.

[22] P. Wu, K. Gan, D. Yan, Z. Fu, Z. Li, A non-equiatomic FeNiCoCr high-entropy alloy with excellent anti-corrosion performance and strength-ductility synergy, Corrosion Sci. 183 (2021) 109341, https://doi.org/10.1016/j.corsci.2021.109341.

[23] Y.J. Liang, L. Wang, Y. Wen, B. Cheng, Q. Wu, T. Cao, Q. Xiao, Y. Xue, G. Sha, Y. Wang, High-content ductile coherent nanoprecipitates achieve ultrastrong high-entropy alloys, Nat. Commun. 9 (1) (2018) 4063, https://doi.org/10.1038/s41467-018-06600-8.

[24] A. Poulia, E. Georgatis, C. Mathiou, A. Karantzalis, Phase segregation discussion in a Hf25Zr30Ti20Nb15V10 high entropy alloy: the effect of the high melting point element, Mater. Chem. Phys. 210 (2018) 251–258, https://doi.org/10.1016/j.matchemphys.2017.09.059.

[25] P. Cao, H. Huang, S. Jiang, X. Liu, H. Wang, Y. Wu, Z. Lu, Microstructural stability and aging behavior of refractory high entropy alloys at intermediate temperatures, J. Mater. Sci. Technol. 122 (2022) 243–254, https://doi.org/10.1016/j.jmst.2021.12.057.

[26] Y. Zhang, Y.J. Zhou, J.P. Lin, G.L. Chen, P.K. Liaw, Solid-solution phase formation rules for multi-component alloys, Adv. Eng. Mater. 10 (6) (2008) 534–538, https://doi.org/10.1002/adem.200700240.

[27] S. Sheikh, S. Shafeie, Q. Hu, J. Ahlström, C. Persson, J. Veselý, J. Zýka, U. Klement, S. Guo, Alloy design for intrinsically ductile refractory high-entropy alloys, J. Appl. Phys. 120 (16) (2016) 164902, https://doi.org/10.1063/1.4966659.

[28] T. Nagase, M. Todai, P. Wang, S.H. Sun, T. Nakano, Design and development of (Ti, Zr, Hf)-Al based medium entropy alloys and high entropy alloys, Mater. Chem. Phys. 276 (2022) 125409, https://doi.org/10.1016/j.matchemphys.2021.125409.

[29] M.H. Tsai, J.H. Li, A.C. Fan, P.H. Tsai, Incorrect predictions of simple solid solution high entropy alloys: cause and possible solution, Scr. Mater. 127 (2017) 6–9, https://doi.org/10.1016/j.scriptamat.2016.08.024.

[30] A. Roy, T. Babuska, B. Krick, G. Balasubramanian, Machine learned feature identification for predicting phase and Young's modulus of low-, medium-and high-entropy alloys, Scr. Mater. 185 (2020) 152–158, https://doi.org/10.1016/j.scriptamat.2020.04.016.

[31] G. Sheng, C.T. Liu, Phase stability in high entropy alloys: formation of solid-solution phase or amorphous phase, Prog. Nat. Sci. Mater. Int. 21 (6) (2011) 433–446, https://doi.org/10.1016/S1002-0071(12)60080-X.

[32] M.G. Poletti, L. Battezzati, Electronic and thermodynamic criteria for the occurrence of high entropy alloys in metallic systems, Acta Mater. 75 (2014) 297–306, https://doi.org/10.1016/j.actamat.2014.04.033.

[33] J.O. Andersson, T. Helander, L. Höglund, P. Shi, B. Sundman, Thermo-Calc & DICTRA, computational tools for materials science, Calphad 26 (2) (2002) 273–312, https://doi.org/10.1016/S0364-5916(02)00037-8.

[34] E. Scheil, Bemerkungen zur schichtkristallbildung, Int. J. Mater. Res. 34 (3) (1942) 70–72, https://doi.org/10.1515/ijmr-1942-340303.

[35] G. Gulliver, The quantitative effect of rapid cooling upon the constitution of binary alloys, J. Inst. Met. 13 (1915) 263–291.

[36] T. Nagase, M. Todai, T. Hori, T. Nakano, Microstructure of equiatomic and non-equiatomic Ti-Nb-Ta-Zr-Mo high-entropy alloys for metallic biomaterials, J. Alloy. Compd. 753 (2018) 412–421, https://doi.org/10.1016/j.jallcom.2018.04.082.

[37] T. Hori, T. Nagase, M. Todai, A. Matsugaki, T. Nakano, Development of non-equiatomic Ti-Nb-Ta-Zr-Mo high-entropy alloys for metallic biomaterials, Scr. Mater. 172 (2019) 83–87, https://doi.org/10.1016/j.scriptamat.2019.07.011.

[38] B. Zhang, M. Gao, Y. Zhang, S. Guo, Senary refractory high-entropy alloy CrxMoNbTaVW, Calphad 51 (2015) 193–201, https://doi.org/10.1016/j.calphad.2015.09.007.

[39] O. Senkov, G. Wilks, D. Miracle, C. Chuang, P. Liaw, Refractory high-entropy alloys, Intermetallics 18 (9) (2010) 1758–1765, https://doi.org/10.1016/j.intermet.2010.05.014.

[40] H. Yao, J. Qiao, M. Gao, J. Hawk, S. Ma, H. Zhou, Y. Zhang, NbTaV-(Ti, W) refractory high-entropy alloys: experiments and modeling, Mater. Sci. Eng. A 674 (2016) 203–211, https://doi.org/10.1016/j.msea.2016.07.102.

[41] K. Ming, L. Li, Z. Li, X. Bi, J. Wang, Grain boundary decohesion by nanoclustering Ni and Cr separately in CrMnFeCoNi high-entropy alloys, Sci. Adv. 5 (12) (2019) eaay0639, https://doi.org/10.1126/sciadv.aay0639.

[42] O. Senkov, J. Scott, S. Senkova, D. Miracle, C. Woodward, Microstructure and room temperature properties of a high-entropy TaNbHfZrTi alloy, J. Alloy. Compd. 509 (20) (2011) 6043–6048, https://doi.org/10.1016/j.jallcom.2011.02.171.

[43] S.P. Wang, J. Xu, (TiZrNbTa)-Mo high-entropy alloys: dependence of microstructure and mechanical properties on Mo concentration and modeling of solid solution strengthening, Intermetallics 95 (2018) 59–72, https://doi.org/10.1016/j.intermet.2018.01.017.

[44] L. Gypen, A. Deruyttere, Multi-component solid solution hardening: part 1 proposed model, J. Mater. Sci. 12 (1977) 1028–1033, https://doi.org/10.1007/BF00540987.

[45] A. Yamamoto, R. Honma, M. Sumita, Cytotoxicity evaluation of 43 metal salts using murine fibroblasts and osteoblastic cells, J. Biomed. Mater. Res. 39 (2) (1998) 331–340, https://doi.org/10.1002/(SICI)1097-4636(199802)39:2%3C331::AID-JBM22%3E3.0.CO;2-E.

[46] C. Wang, Y. Yu, J. Yu, Y. Zhang, F. Wang, H. Li, Effect of the macro-segregation on corrosion behavior of CrMnFeCoNi coating prepared by arc cladding, J. Alloy. Compd. 846 (2020) 156263, https://doi.org/10.1016/j.jallcom.2020.156263.

[47] L. Huang, X. Wang, B. Huang, X. Zhao, H. Chen, C. Wang, Effect of Cu segregation on the phase transformation and properties of AlCrFeNiTiCux high-entropy alloys, Intermetallics 140 (2022) 107397, https://doi.org/10.1016/j.intermet.2021.107397.

[48] Y. Shi, L. Collins, R. Feng, C. Zhang, N. Balke, P.K. Liaw, B. Yang, Homogenization of AlxCoCrFeNi high-entropy alloys with improved corrosion resistance, Corrosion Sci. 133 (2018) 120–131, https://doi.org/10.1016/j.corsci.2018.01.030.

[49] T. Ishimoto, R. Ozasa, K. Nakano, M. Weinmann, C. Schnitter, M. Stenzel, A. Matsugaki, T. Nagase, T. Matsuzaka, M. Todai, H.S. Kim, T. Nakano, Development of TiNbTaZrMo bio-high entropy alloy (BioHEA) super-solid solution by selective laser melting, and its improved mechanical property and biocompatibility, Scr. Mater. 194 (2021) 113658, https://doi.org/10.1016/j.scriptamat.2020.113658.